S1. Apparatus and experiment setup

The apparatus of the robotic swimmer device is shown in Fig. S1a. The swimmer rests on a set of three kinematic mounts. Each mount is a 25mm $\times$ 25mm $\times$ 25mm aluminum cube that was CNC machined at Georgia Tech's Montgomery Machining Mall using a Dayton Mill Drill Machine. One mount has a ball and socket groove (constrains 3 degrees of freedom for motion), another has a grooved slot (constrains 2 degrees of freedom for motion), and the last has a smooth surface (constrains 1 degree of freedom for motion). These mounts were fixed to the ground with super glue. Having the three kinematic mounts ensures that the device has all six degrees of freedom for motion constrained, preventing slipping or wobbling.

The triangular base of the swimmer was machined out of 0.25 inch aluminum using a Maxiem CNC Waterjet at Georgia Tech's Flowers Invention Studio. The base is an equilateral triangle with sides that are 550 mm long. The base also has 3 holes (one at each corner) that have a thread brass insert inside. A 0.25-inch-100-thread ultra-high precision set screw is placed inside each brass insert, and the tip of each set screw rests on one of the kinematic mounts. These set screws can be adjusted to make minute changes in the angle of the base.

The side panels are machined the same way as the base and are attached to the base using M5 bolts and corner brackets so that they stand up vertically. In between the side panels, there are two 25 mm diameter air bushings secured in the mounting boxes. When connected to air, the air bushings blow tiny streams of air radially inward so that any rod inside of them is left "floating" inside with minimal friction. Inside the air bushings, there is a 25 mm diameter steel shaft that is 450 mm tall. The bottom of the rod rests on a 25 mm diameter flat air bearing mounted to the center of the triangular base. Using the combination of two bushings and a bearing, the steel shaft is supported vertically with minimal friction and allowed to rotate freely. The air bushings, air bearings, and mounting boxes were from New Way Air Bearings.

On top of the steel shaft is a T-Shaped connector that was 3D-printed in PLA (polylactic acid) plastic using an Ultimaker S3 3D Printer at Georgia Tech's FLower's Invention Studio. The connector has two holes that are perpendicular to one another. The bottom hole is rigidly fastened to the steel shaft using nuts and bolts. In the other hole of the Connector there is a 15 mm diameter carbon fiber arm, that extends out 400 mm, which stays

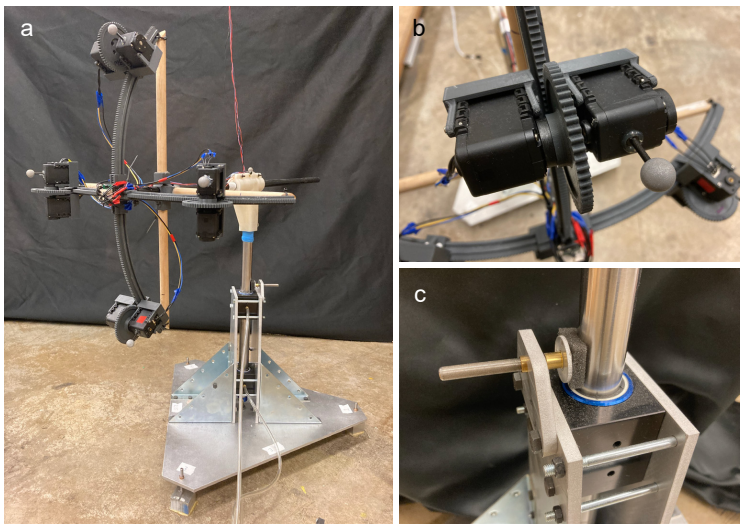

Figure S1: Apparatus and experiment setup of the swimmer. (a) The swimmer. (b) The motor module. (c) The tunable friction block.

perpendicular to the steel shaft and parallel to the ground. At the end of this carbon fiber arm are the tracks and motors of the swimmer.

Each curved track has a center of curvature at the point where the steel shaft and carbon fiber arm meet and a radius of curvature of 400 mm (same as the length the carbon fiber arm extends out). Each has an arc length of 280 mm (forms an angle of 0.7 rad). The four curved tracks are all connected in the middle of the rod on a connector piece. Each track has teeth running along the outside. Traveling on each track is a motor module (Fig. S1b). The module features a mount that the AX-12A servo motor (from ROBOTIS) is rigidly attached to using screws and a gear that is rigidly attached to the motor. The gear's teeth line up with the teeth on the track allowing the motor to travel up and down the curve. Opposite each AX-12A servo motor is a counterweight with a weight equivalent to the AX-12A servo motor that moves along the track with the motor. The four curved tracks, the connector, the four gears, and the four motor mounts were printed in ABS (acrylonitrile butadiene styrene) plastic using a Stratasys uPrint SE Plus Printer. To support the tracks there are four 15 mm diameter wooden dowel rods that extend from the carbon fiber arm to the end of each curved track ($\sim$25 mm tall). Wooden rods stabilize the tracks and prevent unwanted shaking.

The four AX-12A servo motors are all connected to a USB communication

converter U2D2 (from ROBOTIS) using long soft wires so that the U2D2 does not rest on the swimmer. The wires remain loose and do not interfere with the swimming motion. The servo motors are controlled by position commands via TTL Communication.

A polyurethane foam is attached to the shaft to create tunable friction on the swimmer. The foam is fixed on a sliding block (Fig. S1c), which allows us to adjust the normal force, therefore the friction, by adjusting the set screw.

To track the motion of the swimmer in its position space, six IR reflective markers were attached and tracked the trajectories of the markers using an OptiTrack motion capture system with six OptiTrack Flex 13 cameras. Four markers were attached to the motor modules, one was attached to the pivot position on the T-connector, and the other one is attached on the carbon fiber arm. Real-time 3D positions of the markers were captured at a 120 FPS frame rate.

S2. Gait execution

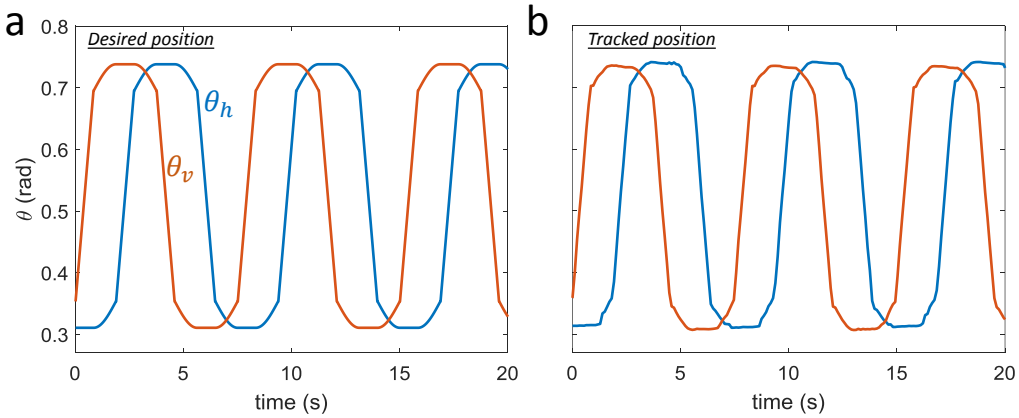

Figure S2: Commanded positions (a) sent to servo motors and the tracked motor positions (b).

To avoid mechanical instability, we smooth the connection between the piecewise strokes with sinusoidal functions. Fig. S2a shows an example of the desired θ_v and θ_h for the gait with $\varphi_d = -\pi/2$ positions. In the experiment, the rotary motor was controlled by the angular positions of its wheel gear. Since the relation between θ_v (θ_h) and the position of a vertical (horizontal) motor on the track is linear, and the motor position on the track is proportional to the angular position of the motor wheel gear, the position commands to motors were derived from θ_v and θ_h by a simple linear mapping. The swimmer executes the gait when all motors follow the sequences of position commands. Fig. S2b shows the θ_v and θ_h observed from the motion tracking system to show the quality of gait execution.

In each experiment, we executed the same sequence of gaits on the swimmer: the null gait, the swimming gait, and the null gait again. The first null gait corresponds to the null stage in Fig. 4(a); the swimming gait corresponds to the swimming and the plateau stages; and the second null gait corresponds to the negative momentum stage. We switched from the null gait to the swimming gait at $t = 170$ s and switched back to the null gait at $t = 920$ s.

Notice that there is a stage transition (from swimming to plateau) during the swimming gait. We chose the transition point between the swimming

and the plateau stages following the rule that – in experiment, the absolute value of the difference between the time-averaged position at the current time step, $\bar{\phi}(t_k)$, and the time-averaged position at the previous time step, $\bar{\phi}(t_{k-1})$, is less than a certain threshold, γ, for a certain time span, $T^{\text{transition}}$. In all results presented in the manuscript, we calculated $\bar{\phi}$ at a 30 Hz frequency and set γ to be 10^{-4} rad and $T^{\text{transition}}$ to be 30 s. The choices of the thresholding parameters were experimentally determined. The results are qualitatively robust to changes in these choices within a reasonable range.

S3. Equation of motion

The total angular momentum of the swimmer is composed of three parts: the contribution from the vertical motors, the horizontal motors, and the track system supporting the motors together with the supporting rod.

$$\begin{aligned} L &= L_{\text{vertical}} + L_{\text{horizontal}} + L_{\text{track}} && (1)\\ &= 2m_v R_0^2 \cos^2\theta_v \dot{\phi} + 2m_h R_0^2(\dot{\theta}_h + \dot{\phi}) + I_{\text{track}}\dot{\phi} && (2) \end{aligned}$$

If we collect the terms with $\dot{\phi}$ together, we have (following the "shape dynamics" section of the Methods)

$$L = I\dot{\phi} + \dot{\alpha} \tag{3}$$

where now

$$\begin{aligned} I(t) &= 2m_v R_0^2 \cos^2\theta_v(t) + 2m_h R_0^2 + I_{track}, && (4)\\ \alpha(t) &= 2m_h R_0^2 \theta_h(t). && (5) \end{aligned}$$

The torque that changes the angular momentum is composed of two parts, being the contribution from the slight residual gravity and Coulomb friction.

$$\frac{dL}{dt} = \tau = A_g + A_C \tag{6}$$

The force from the residual gravity is caused by the mass of the swimmer on the equator, which normal slightly misaligns with the direction of Earth's gravity with an angle of θ_g. The residual gravity potential contributed by the two horizontal motors, two vertical motors, and the track compose a total residual potential energy of $V = -(2m_v + 2m_h + m_{\text{track}})gR_0 \sin\theta_g \cos(\phi - \phi_0)$. This leads to a torque of

$$A_g = -\partial V/\partial\phi = -(2m_v + 2m_h + m_{\text{track}})gR_0 \sin\theta_g \sin(\phi - \phi_0) \tag{7}$$

where ϕ_0 is the azimuthal position with the lowest potential energy. Without loss of generality, we set $\phi_0 = 0$ so the torque from gravity and assume ϕ is small and finally arrive at $A_g = -\tau_g\phi$ where $\tau_g = m_s g R_0 \sin\theta_g$ where $m_s = 2m_v + 2m_h + m_{\text{track}}$.

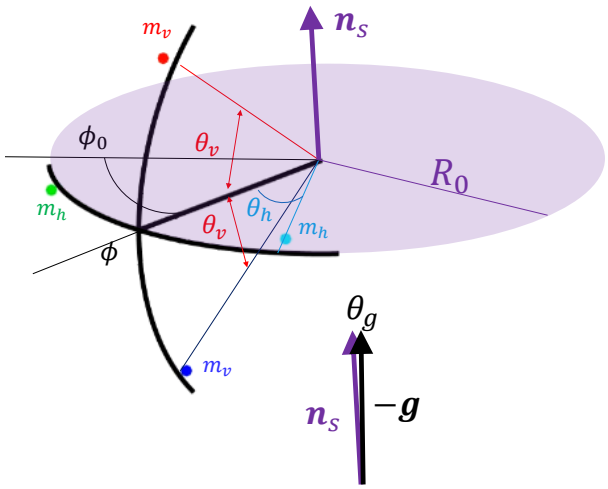

Figure S3: **Setup of the swimmer.** The swimmer with two horizontal motors (each with mass m_h) and two vertical motors (each with mass m_v) rotates about $\mathbf{n}_s$, the normal of the equator shown as the light purple plate. The position of the swimmer, ϕ, the azimuthal angle of the beam arm connecting the center and the curved track arms, evolves as the positions of the motors (θ_h, θ_v) move. Ideally, the normal of the equator $\mathbf{n}_s$ should be aligned with the opposite direction of gravity $-\mathbf{g}$. In realistic experiment, we characterize the small residual gravity by the angle θ_g ($\sim 10^{-4}$ rad) between $\mathbf{n}_s$ and $-\mathbf{g}$. We denote the minimal position of the gravity potential as ϕ_0.

The torque from friction has a constant magnitude τ_C and a direction opposite to the angular velocity so

$$M_C = -\tau_C \mathrm{sgn}(\dot{\phi}) \tag{8}$$

Piecing all above, we have the equation of motion as

$$L = I\dot{\phi} + \dot{\alpha} \tag{9}$$
$$\dot{L} = -\tau_C \mathrm{sgn}\dot{\phi} - \tau_g \phi \tag{10}$$

where $\tau_g = (2m_v + 2m_h + m_{\mathrm{track}})gR_0 \sin\theta_g$.

S4. Friction characterization

To characterize and measure the friction, we tracked the decay rate of angular velocity as shown in Fig.S4a. Fig.S4b, an example of such experiment, shows the instantaneous decay rate a_C as a function of the angular velocity $\dot{\phi}$. We note that it is reasonably anti-symmetric about zero, giving a symmetric friction status such that the possible ratchet effect, which could introduce unwanted swimming, is nominal. When reporting the friction in the main text, we use the acceleration evaluated for the range of angular velocity between 0.175 rad/s and 0.035 rad/s, which is the typical range of angular velocity in the swimmer's experiments. To average out the possible slight gravity residue effect, we performed experiments at 5 different azimuthal positions evenly spaced in $(0, 2\pi)$. To avoid the ratchet effect, we only performed swimmer experiments when the discrepancy of friction between the clockwise and counterclockwise value is less than 10 %.

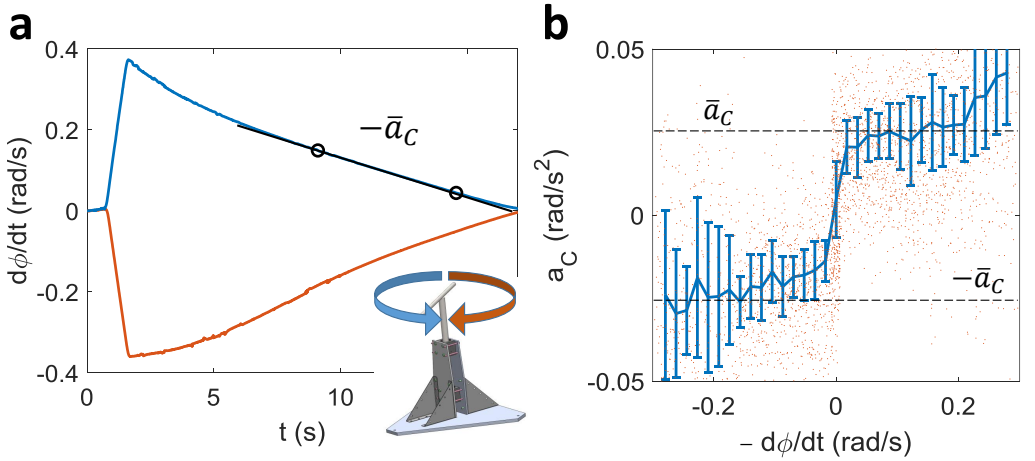

Figure S4: (a) The decay of angular velocity $\dot{\phi}$ over time in experiment. (b) Angular acceleration over $\dot{\phi}$. The orange dots show the raw data. The blue error bars show the median and the middle quartiles of the binned data.

To convert the acceleration to the torque from friction τ_C, we multiply the average acceleration magnitude $\bar{a}_C$ by the total moment of inertia of the swimmer $I_0 = m_s R_0^2$ where m_s, R_0 are the mass and the radius of the swimmer, respectively.

S5. Inferring the slight gravity potential

Since the gravity potential well from the slight tilting of the equator is so shallow that direct measurement from devices such as bubble meter or optic tracking does not have sufficient resolution due to possible error from the mounting of trackers, we infer its depth using the long oscillation period resulted from it.

Particularly, we perform a very long null gait in which only the horizontal motor moves. The averaged ϕ (i.e., the envelope $\bar{\phi}$) is given by Eq. (4) in the main text as

$$\langle I^{(0)}\rangle\ddot{\bar{\phi}} = -\frac{4\tau_{\mathrm{C}}\langle I^{(0)}\rangle}{T|\ddot{\alpha}|}\left[\dot{\bar{\phi}} - \omega_g\right] - \tau_g\bar{\phi}. \tag{11}$$

where $\omega_g = 0$ since there is no geometric phase enclosed. Given that the moment of inertia is fixed as $I_0 = m_s R_0^2$ in the null gait and $\alpha = 2m_v R_0^2\theta_h$, the equation for the long-time envelope is, therefore

$$I_0\ddot{\bar{\phi}} = -\frac{2\tau_{\mathrm{C}}m_s}{Tm_v|\ddot{\theta}_h|}\dot{\bar{\phi}} - \tau_g\bar{\phi}. \tag{12}$$

When τ_C is relatively small, the oscillation period of $\bar{\phi}$, T_{env}, is approximately $(2\pi/T_{\mathrm{env}})^2 = \tau_g/I_0$ where $\tau_g = m_s g R_0 \sin\theta_g$ and $I_0 = m_s R_0^2$. This implies

$$\theta_g \approx \sin\theta_g = \frac{R_0}{g}\left(\frac{2\pi}{T_{\mathrm{env}}}\right)^2. \tag{13}$$

With $R_0 = 0.46$ m, from an experiment with null gait and small friction $\tau = 0.003$ kg m^2 s^{-2}, we can see the period of the envelope T_{env} is about 120 s and thus inferring a residual gravity of $\theta_g = 1.2 \times 10^{-4}$ rad.

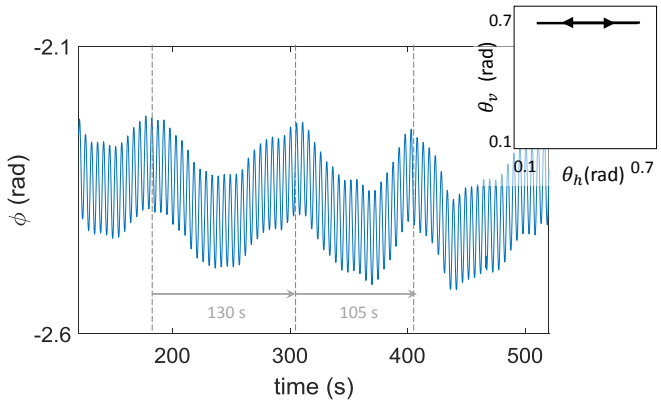

Figure S5: **Inferring the gravity residue.** The residual gravity angle is inferred from the long-time envelope of a null gait experiment with small friction ($\tau = 0.003$ kg m^2 s^{-2}).

S6. Numerical integration

To obtain the equation for numerical integration, we plug the angular momentum Eq.3 into the equation of motion Eq.10, so

$$-\tau_C \mathrm{sgn}(\dot{\phi}) - \tau_g \phi = \frac{dL}{dt} \tag{14}$$

$$= \frac{dI}{dt}\dot{\phi} + I\ddot{\phi} + \ddot{\alpha} \tag{15}$$

$$= \frac{\partial I}{\partial \theta_v}\dot{\theta}_v\dot{\phi} + I\ddot{\phi} + \ddot{\alpha} \tag{16}$$

Plugging in the $I(\theta_v(t))$ in Eq.4 and the α in Eq.5, we finally arrive at

$$\ddot{\phi} = I(\theta_v)^{-1}\left(2m_v R_0^2 \sin(2\theta_v)\ \dot{\theta}_v\dot{\phi} - 2m_h R_0^2\ddot{\theta}_h - \tau_C \mathrm{sgn}(\dot{\phi}) - \tau_g\theta\right) \tag{17}$$

The numerical simulation integrates Eq.17. The initial position $\phi(0) = 0$ such that the swimmer starts from the bottom of the slight potential well from the residual gravity. The initial angular velocity $\dot{\phi}$ is chosen that the initial angular momentum $L(0) = I(0)\dot{\phi}(0) + \dot{\alpha}(0)$ is zero.

The motor positions $\theta_v(t)$ and $\theta_h(t)$ use the commanded signal sent to the motor (see Fig.S1). The sign function in the Coulomb friction is smoothed

by the arctan function with characteristic angular speed 0.01 rad/s $\ll$ the typical speed of the swimmer to avoid the numerical singularity. There are two motors on the horizontal track and two motors on the vertical track. The mass of each motor is 0.116 kg $= m_v = m_h$. The radius of the swimmer is $R_0 = 0.46$ m. The mass the track is $m_{\text{track}} = 0.388$ kg.

For the convenience of implementing the same gait as the commanded shape change sent to the motors, which are discrete signals requiring interpolation in the differential equations to be integrated, we use a numerical scheme with fixed steps (forward Euler) so that the interpolation of the input signal is time-economic. The test of convergence with step size h shows a global (i.e. position ϕ) error of $O(h)$ (and therefore local error of $O(h^2)$) as expected for a first-order scheme. We use the step size $h = 3.1 \times 10^{-4}$ s such that the relative error is 1.8 %.

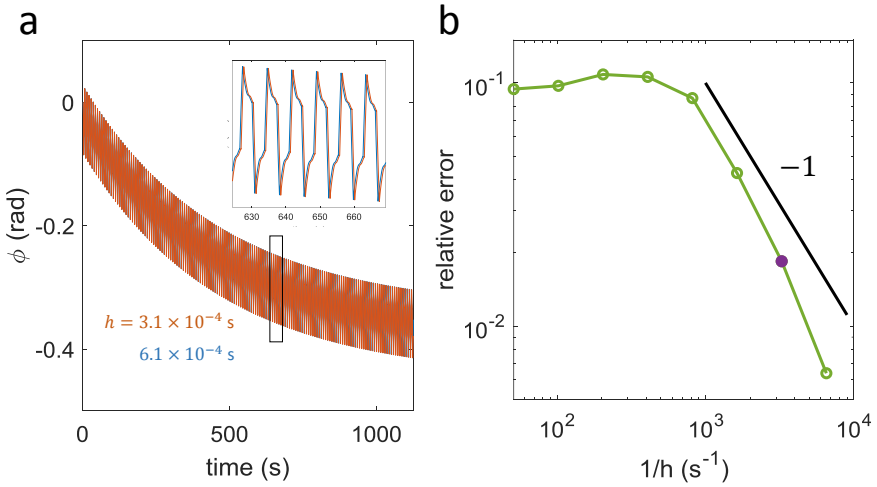

Figure S6: **Numerical convergence check.** (a) Numerical integration of a swimmer driven by a square swimming gait and subjected to a friction of $\tau_C = 8.6 \times 10^{-3}$ kg m^{2}s^{-2} and residual gravity $\tau_g = 4.0 \times 10^{-4}$ kg m^{2}s^{-2} with step sizes $h = 3.1 \times 10^{-4}$ s and 6.1×10^{-4} s. The inset shows a close-up at around 650 s. (b) The relative error from numerical integration improves with the decrease of step size h. The improvement largely follows a trend of $O(h)$, which can be seen by a comparison with the black line that has a power of -1. Here the relative error is defined as the average of $|\phi_{\text{num}} - \phi_{\text{truth}}|/|\phi_{\text{num}}|$ where we use $h = 7.7 \times 10^{-5}$ s to approximate ϕ_{truth}. The step size we use in this study, $h = 3.1 \times 10^{-4}$, is shown in a solid purple dot.

S7. Plateau and negative momentum

For small L, Eq.4 in the main text gives

$$0 = \frac{1}{\langle I \rangle}\left(-\tau_C \frac{4\bar{L}}{T|\ddot{\alpha}(0)|} - \tau_g \bar{\dot{\phi}}\right) \tag{18}$$

$$\frac{L_{ss}}{\phi_{ss}} = -\frac{\tau_g T|\ddot{\alpha}(0)|}{4\tau_C} = -\frac{g\sin\theta_g T|\ddot{\alpha}(0)|}{4Ra_C} = -\frac{gR\sin\theta_g T m_h|\ddot{\theta}_h(0)|}{2a_C} \tag{19}$$

To evaluate the angular momentum $L = I(t)\dot{\phi} + \dot{\alpha}$, we compute with all components $(\phi(t), I(t) = 2m_v R^2\cos^2\theta_v(t) + 2m_h R^2 + I_{\text{track}}R^2, \alpha(t) = 2m_h R^2\theta_h(t))$ from experimentally recorded data. As the raw angular momentum is expected to have large fluctuation, we filter it with a Gaussian filter with width $\sigma = T$. The steady-state values of angular momentum and ϕ, which are L_{ss} and ϕ_{ss} use the average of the last 80% in swimming stage since the incipient part is transient.

We also want to note that the characteristic high friction $\tau_{C0} = |\ddot{\alpha}| = 2m_h R^2|\ddot{\theta}_h|$ where $|\ddot{\theta}_h| = 0.12$ rad/s^2 (which can be read from Fig. S2).

In fact, if we consider a moment t where $L(t) = \dot{\alpha}(t)$, then after a short time δt,

$$\delta(I\dot{\phi}) = \delta(L - \dot{\alpha}) \tag{20}$$

$$= \dot{L}\delta t - \ddot{\alpha}\delta t. \tag{21}$$

For a large τ_C that we can neglect τ_g so that $\dot{L} = -\tau_C \text{sgn}(\dot{\phi})$, we have

$$\delta(I\dot{\phi}) = (\pm\tau_C - \ddot{\alpha})\delta t. \tag{22}$$

This indicates that when $\tau_C > |\ddot{\alpha}|$, the steady state ϕ cannot be further improved.

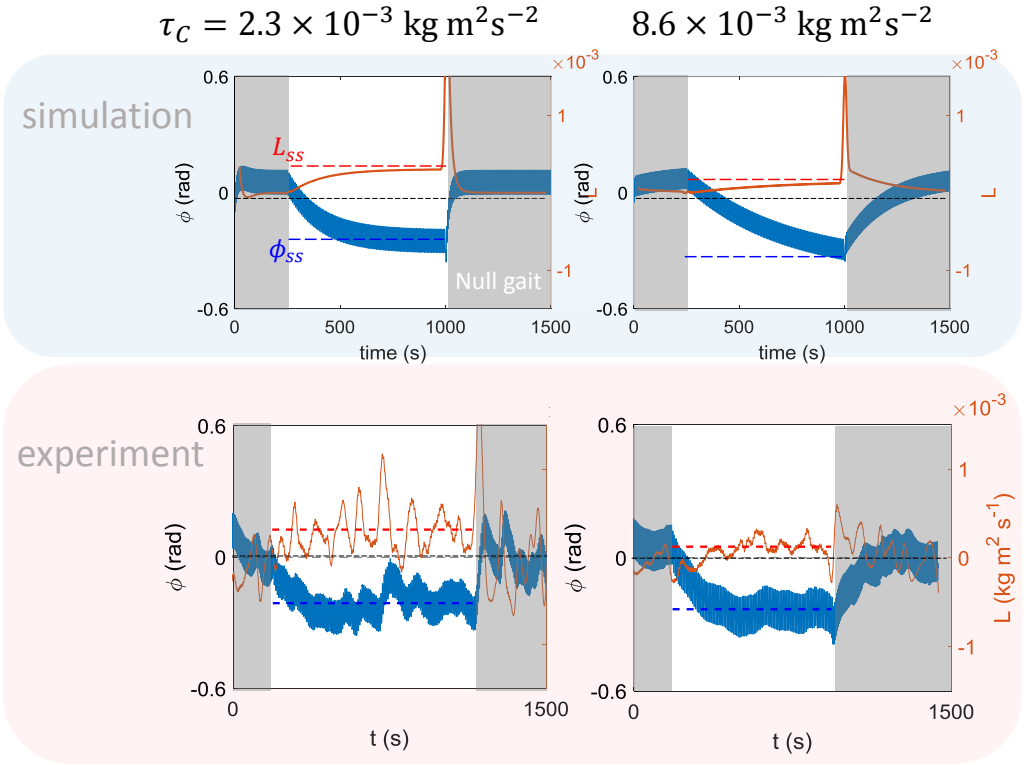

Figure S7: **Simulation of negative momentum.** Note that the L_{ss} gets smaller with the torque of friction τ_C.

S8. Swimmer on generic surfaces with axial and mirror symmetries

Here we consider a generic surface with axial and mirror symmetries with mass distribution shown in Fig.S8a. We can describe the shape by the radius R over z, the vertical coordinate in a cylindrical coordinate system. Alternatively, R can be also viewed as a function over ℓ_v, the geodesic distance between the vertical mass and the center of the swimmer. We denote $R(z=0) = R(\ell_v = 0) = R_0$.

The kinetic energies of each horizontal mass and vertical mass with mass m are

$$T_h = \frac{m}{2} R_0^2 (\dot{\phi} + \dot{\ell}_h)^2 \tag{23}$$

$$T_v = \frac{m}{2} (R^2 \dot{\phi}^2 + \dot{\ell}_v^2) \tag{24}$$

If we assume there is no external potential or friction, the Euler-Langrange of $\mathcal{L} = 2(T_h + T_v)$ gives

$$\dot{\phi} = \frac{R_0^2}{R_0^2 + R^2} \dot{\ell}_h + 0 \dot{\ell}_v \tag{25}$$

Therefore, the net displacement over one cycle is

$$\Delta\phi = \oint \frac{R_0^2}{R_0^2 + R^2} d\ell_h \tag{26}$$

$$= \iint -\frac{R_0^2}{(R_0^2 + R^2)^2} \frac{\partial R^2}{\partial \ell_v} d\ell_h d\ell_v \tag{27}$$

In conclusion, we can see that the Berry phase $\Delta\phi$ can be viewed as an effective scalar curvature field κ_{eff} integrated in the shape space.

$$\kappa_{\text{eff}} = -\frac{R_0^2}{(R_0^2 + R^2)^2} \frac{\partial R^2}{\partial \ell_v}, \ \Delta\phi = \iint \kappa_{\text{eff}} d\ell_h d\ell_v \tag{28}$$

where ℓ_h and ℓ_v are the geodesic distances of the horizontal masses and vertical masses from the center of swimmer. R denotes the radius from the

axis to the curvature as a function of ℓ_v and $R_0 \equiv R(0)$. Eq. 28 shows that the sign of κ_{eff}, which largely dictates the direction of motion depends on $R_{,\ell_v}$, which has the same sign as the intrinsic curvature. Fig. S8 shows three representing cases: a sphere, a cylinder, and a hyperboloid with positive, zero, and negative intrinsic curvature respectively. As the swimmer changes its shape through ℓ_h and ℓ_v, the effective curvature enclosed in the trajectory of (ℓ_h, ℓ_v) dictates the direction of motion. In the sphere and hyperboloid case where effective curvature has the same sign everywhere, the swimming per cycle increases with the area of shape space trajectory [Fig. 2(c)], which increases with the phase lag [Fig. 2(b),3(b)].

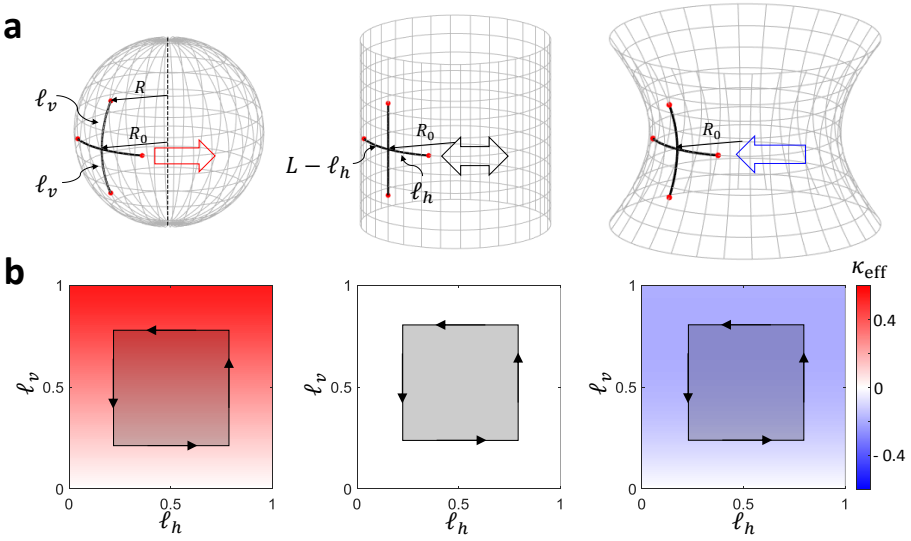

Figure S8: **Enclosed effective curvature dictates the sign and magnitude of swimming for the same gait.** (a) A swimmer moving on a sphere, a cylinder, and a hyperboloid by varying the geodesic distances, ℓ_h and ℓ_v, between the masses (red dots) over time. We choose the radius on the equator unit ($R_0(z = 0) = 1$) and the Gaussian curvatures for the three cases $+1, 0, -1$ respectively. (b) The integral of effective curvature κ_{eff} over the directed area inside the swimmer's trajectory in shape space dictates the direction and magnitude of swimming per cycle. The spherical case here connects to our spherical swimmer tested in experiments with $\ell_h = R_0\theta_h, \ell_v = R_0\theta_v$.

From the above, we can see that the direction of motion is not determined

locally. Instead, it is dictated by the collective contribution of curvature inside the trajectory in the shape space.

S9. Swimmer on helicoid

In this case, the surface coordinates, ρ and θ, map to the Cartesian coordinates: $x = \rho\cos(\alpha\theta), y = \rho\sin(\alpha\theta)$, and $z = \theta$ (the vertical axis), where α is a constant that determines the pitch and handedness of the helicoid about its axis so that geodesics of this surface satisfy the equations of motion:

$$\ddot{\rho} = 2\alpha^2\rho\dot{\theta}, \tag{29}$$

$$\ddot{\theta} = -4\alpha^2\rho(1+\alpha^2\rho^2)\dot{\theta}\dot{\rho}. \tag{30}$$

The radial (r) and lateral (l) servo motors (respectively corresponding to the vertical [v] and horizontal [h] servos on the sphere) can then be prescribed some trajectory along the surface of the helicoid, from which the force-free equation of motion can be determined via angular momentum conservation:

$$\dot{\theta} = -\frac{(1+\alpha^2\rho^2)\dot{\theta}_l}{2+2\alpha^2\rho^2+\alpha^2\rho_r(2\rho+\rho_r)}. \tag{31}$$

In particular, let the radial (r) and lateral (l) servos (respectively corresponding to the vertical [v] and horizontal [h] servos on the sphere) be prescribed sinusoidal gaits in the ρ and θ directions respectively,

$$\theta_l^{\pm}(t) = \frac{1}{8}(1+\cos t) \pm \frac{1}{4}, \quad \rho_r^{\pm}(t) = \pm\frac{1}{8}(1+\sin t), \tag{32}$$

and fix the pitch $\alpha = 1$ along with the radial coordinate of the central joint $\rho = 1/2$. The resulting evolution is shown in Fig. S9, with snapshots along the marked timestamps in Figs. S9C-F.

From Eq.31 we can see that when the Gaussian curvature is zero ($\alpha = 0$), the swimmer cannot swim since Eq.31 reduces to $\dot{\theta} = -\dot{\theta}_t/2$ so that a periodic stretching of limbs (periodic θ_t) does not yield net translation of θ.

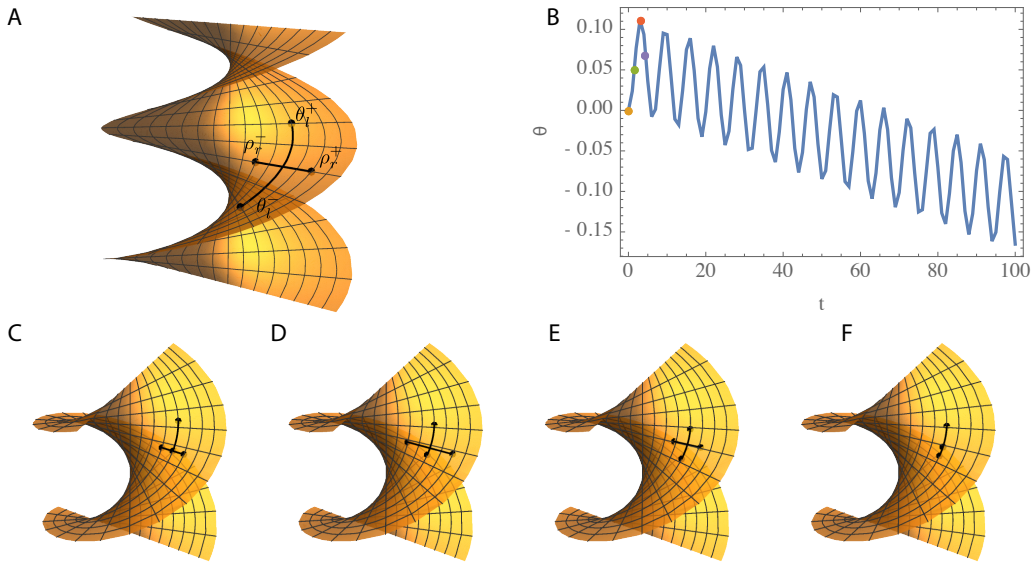

Figure S9: Locomotion along a helicoid: (A) Schematic of the four servos and the surface. (B) Time evolution of the curvature swimmer along the vertical axis ($\theta = z$) of the helicoid. (C-F) Snapshots of the curvature swimmer in order of the four points marked in panel B.

S10. Supplementary Movie

In this video, we show demonstrations of the robot implementing the null gait and the swimming gait, as well as examples of the positive and negative swimming in the 'spherical swimmer' and a comparison to the 'cylindrical swimmer'.